Pergamon

Cement and Concrete Research 29 (1999) 397–406

CEMENT AND CONCRETE RESEARCH

Effects of loading rate on the fracture of cementitious materials[1]

S. Tandon, K.T. Faber *

Department of Materials Science and Engineering, Robert R. McCormick School of Engineering and Applied Science, Northwestern University, Evanston, Illinois 60208-3108, USA

Manuscript received 10 September 1998; accepted manuscript 27 November 1998

Abstract

Cement paste, mortar, and concrete were studied to examine the influence of loading rate on operative toughening mechanisms. The fracture toughness of cement paste was found to be independent of crack length, while mortar and concrete exhibited strongly rising resistance curves. In the case of cement paste and mortar, the peak fracture toughness was found to be independent of the loading rate. In concrete, the peak toughness was found to decrease with increasing loading rate. Surface roughness measurements were performed to understand the effect of loading rate on the fracture mechanisms. The roughness analysis coupled with fractography were found to correlate with the toughness measurements.

Keywords: Cementitious; Fracture; Loading rate; Resistance curves; Surface roughness; Toughness; Toughening mechanisms

The use of cementitious materials in structural applications necessitates an understanding of the response of the material as a function of loading rate, given that a single structure may experience loading, and hence crack growth, at rates that vary over orders of magnitude during its lifetime. In addition to the adhesive or cohesive failure at the tip of a propagating crack, processes away from the crack tip afford considerable toughening of the material and must be included in the description of fracture [1]. Specifically, the processes include crack bridging by unhydrated cement grains and formation of unfractured bridges between offset cracks in cement paste [2] and microcracking [3] and crack bridging by aggregates [4] in mortar and concrete. These processes are known to give rise to resistance (R) curve behavior [1], a schematic of which is shown in Fig. 1. By virtue of the shielding processes, the crack resistance increases from an initial value K_o to a maximum $K_{\max}$ with crack extension when the bridging or microcracking zone reaches a steady state. The maximum or steady state toughness of the material is given by Eq. (1).

$$K_{max} = K_o + \Delta K_{SS} \quad (1)$$

where ΔK_{SS} is the steady state toughening contribution from the process zone phenomena.

A number of issues relating to fracture processes and toughening mechanisms have been investigated in cementitious materials. R-curves have been measured in these materials for different mix compositions [5,6] and specimen geometries [6,7]. The fracture behavior of cementitious materials has been related to fracture surface roughness using confocal microscopy [8], microphotography [9], and topographic imaging [10]. One aspect that remains unexplored is understanding of the effect of the loading rate on the toughening mechanisms in cementitious materials. Although static and quasi-static fracture mechanics is a rate-independent theory, the strength and fracture properties of cementitious materials depend on loading rate [11–14] and are, therefore, of great practical interest. This knowledge is useful in lifetime prediction and the design of tougher cement-based materials.

The intent of this work is to examine first the effect of loading rate on toughening and the evolution of R-curves of cement paste, mortar, and concrete, and second (and more important) the differences in the microstructural aspects of the fracture surface which accompany the change in the loading rate. Load-deformation curves from compact tension specimens were experimentally recorded for a range of loading rates in the quasi-static regime. Based on measured curves K_{Ic}^{s} and $CTOD_c$ of the two-parameter fracture model of Jenq and Shah [6] were computed and R-curves were calculated. Fracture surfaces of tested specimens were subjected to three-

* Corresponding author. Tel.: 847-491-2444; Fax: 847-491-7820; E-mail: k-faber@nwu.edu.

[1] This paper was originally submitted to *Advanced Cement Based Materials*. The paper was received at the Editorial Office of *Cement and Concrete Research* on 10 September 1998 and accepted in final form on 27 November 1998.

0008-8846/99/$–see front matter
PII: S0008-8846(98)00223-3

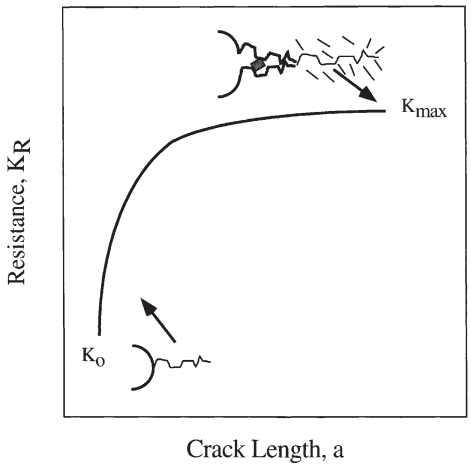

Fig. 1. A schematic of *R*-curve behavior for cementitious materials.

dimensional surface roughness analysis. Finally, the results of toughness measurements and roughness calculations are discussed in conjunction with fractographic analysis.

1. Materials

The materials used for this study—cement paste, mortar, and concrete—were designed and mixed under laboratory conditions. The cement was ASTM Type I portland cement. The sand used for mortar was sieved from ASTM No. 2 sand and ranged in size from 300 to 600 μm. Pea-type gravel, from 3.33 to 4.76 mm, was used for the concrete mix. The mix ratios of all three materials are given in Table 1.

Compact tension specimens were cast following the ASTM C-192 standard [15]. During casting, all of the specimens were compacted by rodding and vibration. During the first 24 h the specimens were left in the molds. Then the specimens were removed and cured in water until the time of testing. A few days before testing, specimens 101.6 × 88.9 × 12.7 mm were ground to make sure that the sides were perpendicular to each other. To achieve conditions of stable crack growth, a chevron notch, perpendicular to and extending 29 mm from the loading axis, was cut using a 250-μm thick diamond wheel (Norton Company, Worcester, MA). Companion cylinders of 76-mm diameter and 152-mm length also were cast for strength measurements. These cylinders were capped with a sulphur compound and were cured under water with the compact tension specimens. The cylinders were used to measure compressive strength (f_c'), and from f_c', determine the elastic modulus (E) of the test materials. The compressive strength and elastic modulus of all the test materials are listed in Table 1.

Table 1
Mix design and properties of the mixes

	Composition	Compressive strength (MPa)	Elastic modulus (GPa)
Cement paste	C:W = 1:0.45	33.8 ± 1.8	27.3 ± 0.8
Mortar	C:S:W = 1:1:0.45	37.5 ± 2.0	29.0 ± 0.8
Concrete	C:S:A:W = 1:1:1:0.45	48.6 ± 6.8	32.9 ± 2.3

C = cement; W = water; S = sand; A = aggregate.

2. Resistance curve measurements

2.1. Test setup and procedure

Notched specimens were tested in displacement control on a servo-electric closed-loop MTS testing machine (Model 808, MTS Corporation, Minneapolis, MN). During each test, load, crosshead displacement, and crack mouth opening displacement (CMOD) were measured and recorded with a data acquisition system. The CMOD, which is the basic indicator of the crack growth in the specimen, was measured by a COD clip gage (MTS, COD GAGE 632.03E-30 Minneapolis, MN). A 100X traveling microscope (Model M101AT, Gaertner Microscope Company, Chicago, IL) equipped with a digital micrometer (Model 164-162, Mitutoyo Corporation, Tokyo, Japan) was used to follow, but not measure, crack growth. Specimens were tested at crosshead displacement rates, designated here as loading rates (v) of 0.25, 1, 10, and 100 μm/min.

The load versus COD curves (shown in Fig. 2 for concrete) show a characteristic linear elastic region prior to peak load (P_u). After peak load, in the softening branch at ~95% P_u, specimens were unloaded to determine the compliance of the loading and unloading branches. After sufficient unloading, the specimens were reloaded to final fracture. The unloading compliance and initial loading compliance were used to calculate values of critical stress intensity factor (K_{Ic}^s) and critical crack tip opening displacement ($CTOD_c$) according to the two-parameter fracture model of Jenq and Shah [6]. The model accounts for nonlinear slow crack growth in cementitious materials prior to the peak load. In this model K_{Ic}^s is calculated at the tip of the effective crack. Crack length of this effective traction-free crack is determined based on the compliance method [16]. According to the model, when a specimen is subjected to its critical fracture load (the peak load), the following two conditions are satisfied [Eq. (2) and Eq. (3)]:

$$K_I = K_{Ic}^S \tag{2}$$

$$CTOD = CTOD_c \tag{3}$$

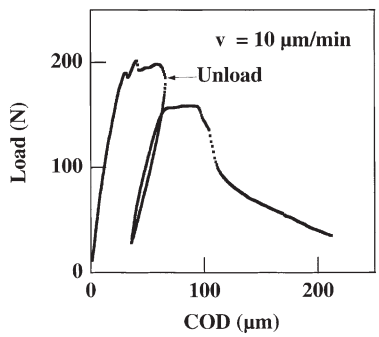

Fig. 2. A representative load versus COD for concrete tested at 10 μm/min.

Using Ouyang and Shah's model [18], *R*-curves for finite size compact tension specimens were calculated. Their model, Eq. (4) defines the *R*-curve as:

$$R = \beta_2 \psi (a - a_o)^{d_2} \quad (4)$$

where β_2, ψ and d_2 are algebraic functions of elastic modulus, crack length, and geometry of the specimens, respectively; a is the crack length and a_o is the notch length. The fracture toughness (K_R) is given by Eq. (5):

$$K_R = \sqrt{RE} \quad (5)$$

where E is the elastic modulus of the material. Combining Eqs. (4) and (5), fracture resistance curves for all three materials tested at different loading rates were calculated.

2.2. Resistance curve results

Table 2 provides the calculated values of K_{Ic}^s and $CTOD_c$ for each of the cement, mortar, and concrete samples tested using the Jenq and Shah model [6]. The $CTOD_c$ values show no specific trend with loading rate for any of the materials. John et al. [17] found $CTOD_c$ values to decrease with loading rate when fracture experiments were conducted over static to dynamic ranges. Little change was seen in the static/quasi-static regime, consistent with the present results. $CTOD_c$ will not be discussed further. Instead we focus on fracture resistance behavior.

2.2.1. Cement paste

Fig. 3 shows the fracture resistance curves for cement paste specimens tested at the loading rate $\nu = 0.25$ μm/min (Fig. 3a) and for $\nu = 10$ μm/min (Fig. 3b). The fracture resistance is independent of crack extension; hence, $K_o = K_{max}$. Similar behavior was observed for the cement specimens tested at 1 and 100 μm/min. K_{max} is plotted against loading rate in Fig. 4a. It is clear that for cement paste K_{max} is independent of the loading rate. The average value of K_{max} for cement paste is 0.2 MPa · $m^{1/2}$.

Table 2
Fracture parameters calculated from the Jenq and Shah [6] model

Material	Loading rate (μm/min)	Specimen ID	Unload point (N)	K_{Ic}^s (MPa • $m^{1/2}$)	$CTOD_c$ (μm)
Cement	0.25	Cement 5	37.73	0.22	4.93
		Cement 8	34.84	0.21	4.87
		Cement 10	35.96	0.23	5.69
	1	Cement 3	37.01	0.20	1.76
		Cement 4	25.51	0.16	1.46
	10	Cement 1	45.97	0.17	1.37
		Cement 2	39.64	0.21	1.78
		Cement 11	43.60	0.18	2.88
	100	Cement 6	27.33	0.18	2.23
		Cement 7	41.89	0.21	4.19
		Cement 12	27.51	0.18	2.57
Mortar	0.25	Mortar 8	112.06	0.43	5.89
		Mortar 11	135.78	0.38	2.84
	1	Mortar 2	132.18	0.41	3.96
		Mortar 4	110.44	0.35	3.52
		Mortar 12	123.30	0.41	4.50
	10	Mortar 1	109.16	0.33	2.06
		Mortar 3	133.34	0.37	8.04
		Mortar 10	150.42	0.48	5.59
	100	Mortar 6	133.83	0.45	5.02
		Mortar 7	88.31	0.38	6.62
		Mortar 9	167.04	0.43	6.15
Concrete	0.25	Concrete 4	249.23	1.12	3.80
		Concrete 8	201.79	1.37	3.82
	1	Concrete 3	190.52	0.86	6.49
		Concrete 7	157.94	1.00	4.30
		Concrete 11	183.24	0.97	3.72
	10	Concrete 1	197.80	0.80	3.59
		Concrete 2	169.74	0.71	3.65
		Concrete 10	185.62	0.77	3.81
	100	Concrete 5	234.77	0.69	4.97
		Concrete 6	159.06	0.45	2.99
		Concrete 9	221.04	0.67	5.22

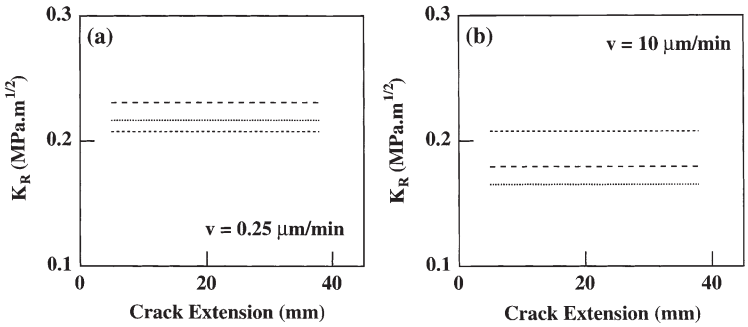

Fig. 3. Fracture resistance curves for cement paste specimens tested at the loading rate $\nu = 0.25$ μm/min (*a*) and for $\nu = 10$ μm/min (*b*).

2.2.2. Mortar

Fracture resistance curves for mortar are shown in Fig. 5 for the two different loading rates. All the specimens of mortar show rising *R*-curve behavior with peak fracture toughness values almost twice that of cement paste, although K_o for mortar is lower than that for paste. This latter feature is a manifestation of the forced fit of $K_o = 0$ at zero crack extension by the Ouyang and Shah model [18]. Such an increase in fracture toughness with crack length derives from microcracking and damage zone formation as shown in Fig. 6a. Unlinked microcracks are seen ahead of the continuous crack tip as noted by an arrow. These unfractured ligaments could be due to bridging sand particles since the size of the bridging ligaments is the same order of magnitude as the size of the sand. K_{max} is plotted against loading rate in Fig. 4b and is also independent of the loading rate. The average value of K_{max} for mortar is 0.4 MPa · $m^{1/2}$.

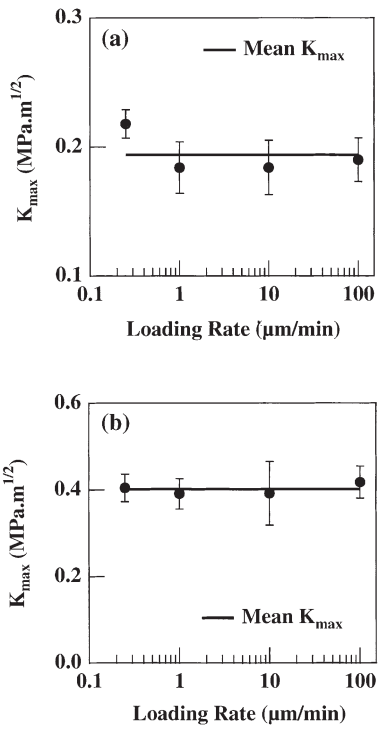

Fig. 4. (*a*) K_{max} plotted against loading rate (for cement specimens). (*b*) K_{max} is plotted against loading rate (for mortar specimens).

2.2.3. Concrete

Fracture resistance curves for concrete are shown in Fig. 7 for the four different loading rates. All the specimens of concrete show rising *R*-curve behavior. Many toughening mechanisms such as crack bifurcation, bridging by unfractured aggregate particles, and aggregate interlocking are operative in concrete. Fig. 6b shows a representative picture of formation of a bridge or offset crack in a concrete specimen. The offset is less than 1 mm and may be due to a subsurface aggregate. K_{max} for concrete is plotted against loading rate in Fig. 8. Unlike paste and mortar, K_{max} decreases with increase in loading rate. At the maximum loading rate of 100 μm/min, K_{max} of concrete approaches that of mortar. At this loading rate it would appear that all the toughening contribution due to aggregate particles is lost and peak toughness is same as that of mortar.

2.3. Oven-dried specimens

It is important to correct for creep effects [19] before the effect of loading rate on the toughening can be fully understood. To eliminate any creep effects, mortar and concrete specimens were oven-dried at 110°C for 36 hours to dry the free water present in the specimens. During the drying process, specimens were weighed at regular intervals to make sure that a stable microstructure was achieved at the end of the drying process [20]. Oven-dried specimens of mortar and concrete were tested at a slow loading rate ($\nu = 0.25$ μm/min) and at a fast loading rate ($\nu = 100$ μm/min). Fig. 9 shows the results of K_{max}, plotted against loading rate for mortar (Fig. 9a) and for concrete (Fig. 9b). Specimens tested at room conditions at the fast loading rate of 100 μm/min take only 1–2 min to fracture. The test time is small and creep during this period can assumed to be negligible. Any difference in toughness between oven-dried and as-cast specimens at the fast loading rate can be assumed due to cracking from oven-drying. However, any difference between the peak fracture toughness of oven-dried specimens with that of as-cast specimens at the slow loading rate (0.25 μm/min) will involve both cracking from oven-drying and creep. For both mortar as well as concrete, we see that the

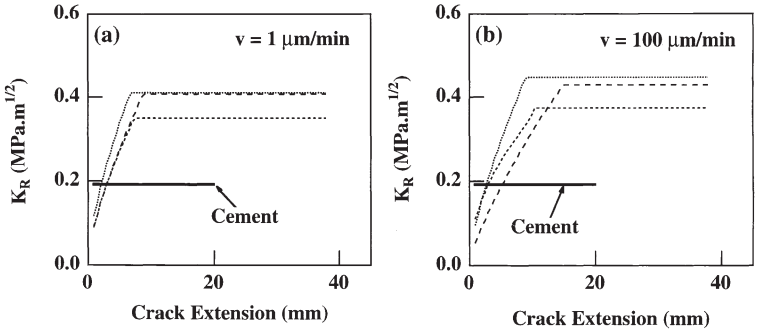

Fig. 5. Fracture resistance curves for mortar for (*a*) $\nu = 1$ μm/min and (*b*) $\nu = 100$ μm/min.

difference between K_{max} of oven-dried specimen and K_{max} of as-cast specimens at fast and slow loading rates is almost the same. Thus, creep effects on the K_{max} for the loading rate range used in these experiments are negligible and the effect of loading rate on K_{max} seen here is definitely a rate-dependent fracture phenomenon.

3. Surface roughness measurements

It has been demonstrated that the fracture properties of ceramic and cementitious materials are related to fracture surface profiles. Mecholsky et al. [21] demonstrated that in the case of alumina and glass-ceramics, the fracture toughness is directly related to the fracture surface roughness. In this study, fracture surfaces of the tested compact tension specimens were analyzed to determine if surface roughness changes with the loading rate. For surface roughness measurements, a 9×9 mm^2 surface area on the fracture surface was chosen in a region of the specimen where a crack was propagating at K_{max}. In one case, a 25×10 mm^2 area in concrete was examined to ascertain the sensitivity of the test to the area measured.

For surface roughness measurements, a coordinate measuring machine (Microval, Brown & Sharpe Manufacturing Company, North Kingston, RI) was used to evaluate a representative fracture area with the appropriate-length scale resolution for cement, mortar, and concrete. During a measurement, specimens were mounted on a stage and the stage was moved in X and Y directions using two micrometers

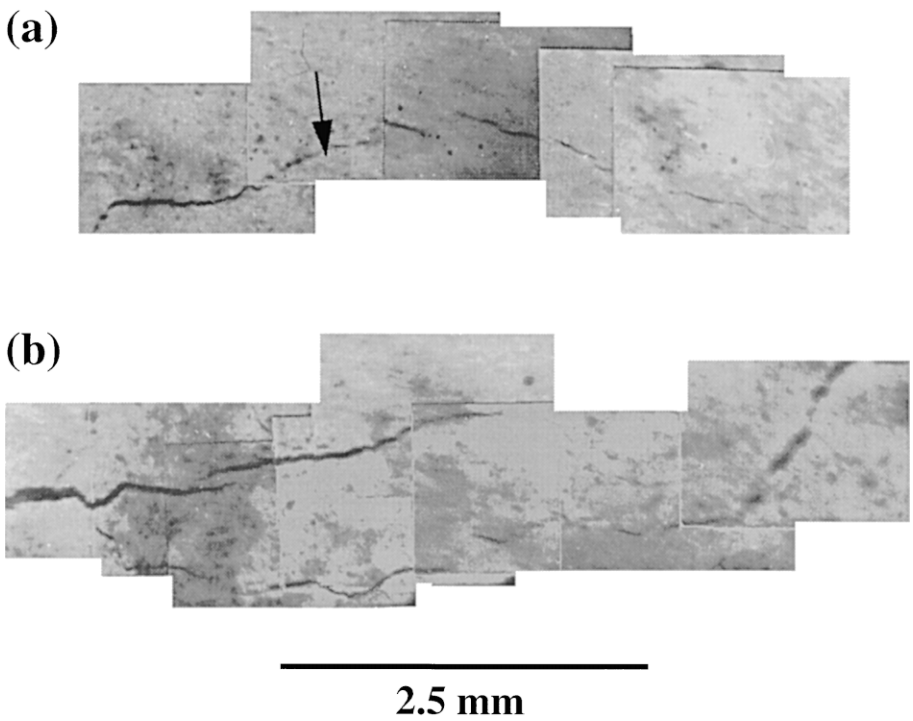

Fig. 6. (*a*) Micrograph of a damage zone in mortar. Unlinked microcracks are seen ahead of the continuous crack tip as noted by an arrow. (*b*) A representative picture of formation of a bridge or offset crack in a concrete specimen.

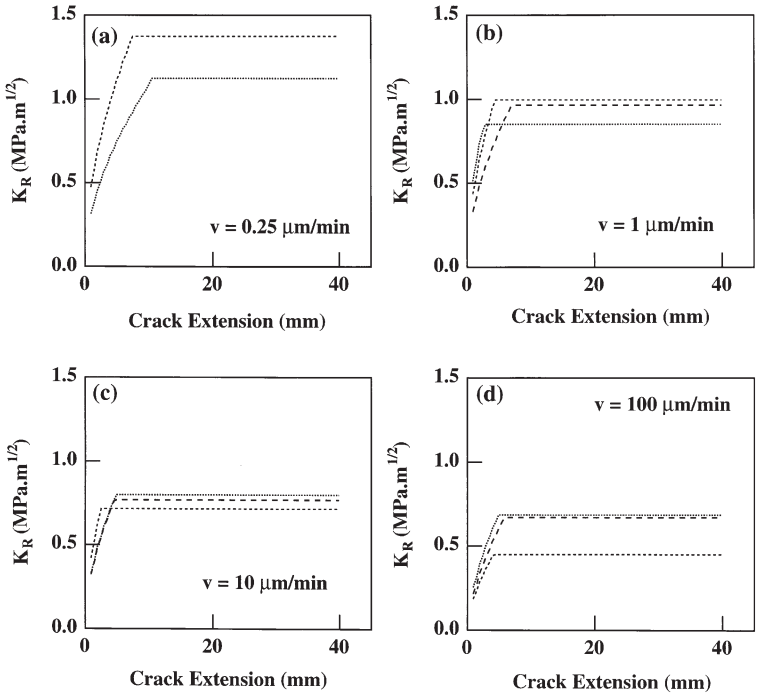

Fig. 7. Fracture resistance curves for concrete at (*a*) $\nu = 0.25$ μm/min, (*b*) $\nu = 1$ μm/min, (*c*) $\nu = 10$ μm/min, and (*d*) $\nu = 100$ μm/min.

and corresponding Z-coordinate was recorded using a touch trigger probe. The probe stylus diameter (Renishaw Incorporated, Schaumburg, IL) was 10 μm and its sensitivity is 1 μm. Each time the probe hits the surface of the specimen, the coordinates are recorded using data acquisition software (Micromeasure III, Brown & Sharpe Manufacturing Company, North Kingston, RI). Approximately 900 coordinate points were measured for any specimen at the regular step size of 300 μm in the X and Y directions. A representative profile of a concrete specimen tested at $\nu = 0.25$ μm/min is shown in Fig. 10a. Due to the presence of aggregate particles, the surface is rough and tortuous, and inclined as well. To correct for the inclination of the fracture surface, a plane is fit to the surface data as shown in Fig. 10b. The best-fit plane is then subtracted from the surface profile and a roughness profile shown in Fig. 11a is derived. Along with this roughness profile, representative roughness profiles of mortar and cement paste specimens tested at 0.25 μm/min are shown in Fig. 11b and 11c, respectively. For visual comparison, all the surface profiles are plotted with the same axis ranges where height is differentiated by color. It is clear

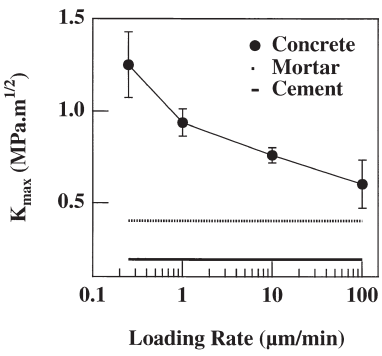

Fig. 8. K_{max} for concrete, plotted against loading rate.

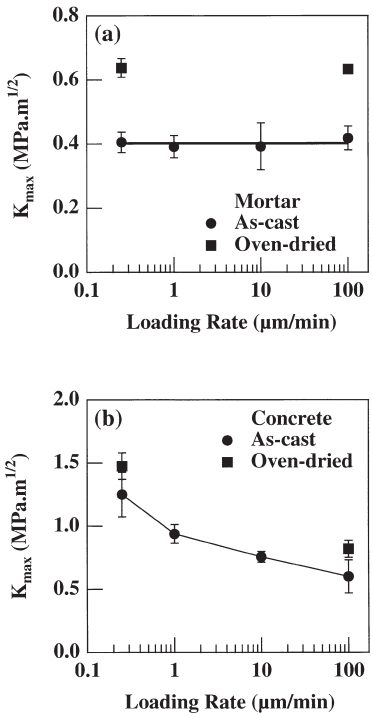

Fig. 9. Results of K_{max}, plotted against loading rate for as-cast and oven-dried (*a*) mortar and (*b*) concrete.

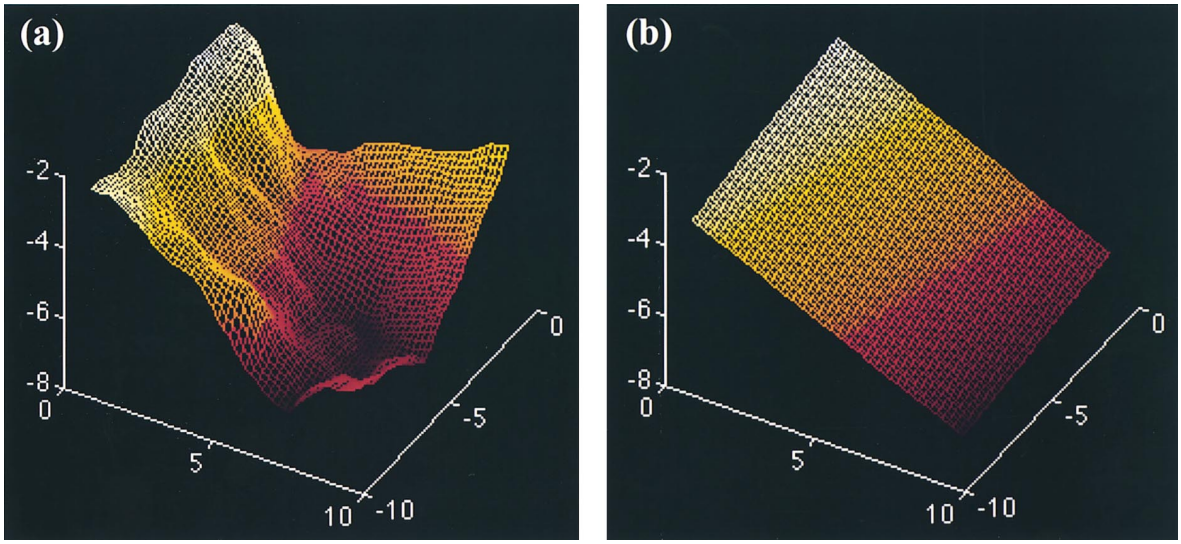

Fig. 10. (*a*) A representative profile of a concrete specimen tested at $v = 0.25$ μm/min. (*b*) To correct for the inclination of the fracture surface, a plane is fit to the surface data.

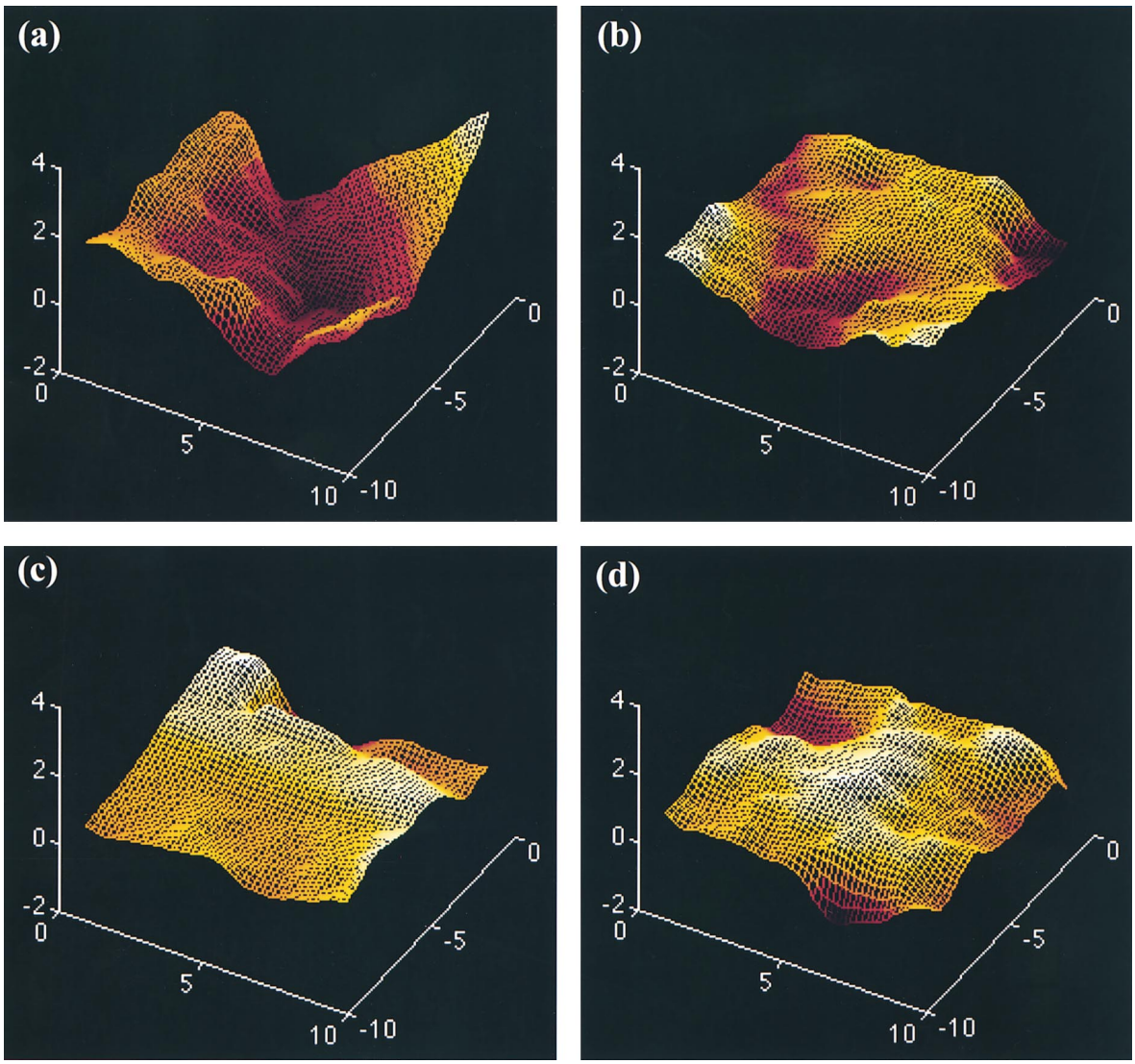

Fig. 11. Roughness profiles for (*a*) concrete, (*b*) mortar, and (*c*) cement paste all tested at 0.25 μm/min. (*d*) For comparison, a roughness profile for concrete tested at 100 μm/min.

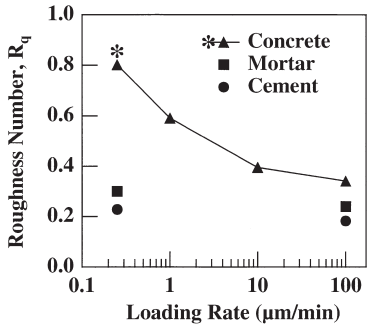

Fig. 12. Summary of results of roughness versus loading rate.

from these profiles that concrete surface is much rougher than the mortar and cement paste surface. For comparison, a concrete specimen surface tested at $\nu = 100$ μm/min is shown in Fig. 11d.

From the roughness profiles, heights from the mean plane were measured and root mean square roughness (R_q) was calculated [22] from Eq. (6):

$$R_q = \sqrt{\frac{h_1^2 + h_2^2 + \ldots + h_n^2}{n}} \quad (6)$$

where h_1, h_2, . . . h_n are heights of the individual coordinate points on the roughness plane and n is the total number of points. Fig. 12 summarizes results of roughness versus loading rate. For cement paste and mortar, roughness values were measured for the specimens tested at the slowest and the fastest loading rates only and shows no change with loading rate. Roughness numbers for mortar specimens are slightly higher than those for cement paste specimens, as expected. For concrete specimens, the roughness number decreases with increase in loading rate. Comparing Fig. 10a with 10d, it is clear the specimen tested at 0.25 μm/min is rougher than the one tested at 10 μm/min by more than a factor of two. For the fast loading rate specimens, surface roughness of concrete specimens approaches the surface roughness of mortar specimens, which is also illustrated by comparison of the roughness profiles shown in Fig. 11b and 11d.

4. Discussion

From the results presented in the preceding sections, it is now documented that net toughness and the associated fracture mechanisms in the cementitious materials depend on the loading rate. With increasing order of complexity of microstructure from cement paste to mortar to concrete, the peak toughness and surface roughness both increase. The greater toughening in mortar and concrete derives from toughening mechanisms active due to the presence of sand and aggregate particles (Fig. 6). Roughness measurements on these materials similarly show a systematic variation with the peak toughness values. Lower values of R_q correspond to lower toughness values, indicative of more brittle behavior. In the case of cement paste and mortar, R_q does not change with loading rate and correlates well with toughness measurements. The rate sensitivity of concrete, in contrast to that of cement paste and mortar, can be further explained through microstructural analysis of the fracture surfaces of the concrete specimens. Fig. 13a shows a representative picture of the fracture surface of a concrete specimen tested at the slow loading rate (0.25 μm/min). Arrows point to the unfractured aggregate particles left behind in the crack wake. The crack runs along the interface between aggregate and matrix material, leaving behind the unfractured aggregate bridge. With these bridging aggregate particles present, full toughening is obtained and a high peak toughness value is observed. For unfractured aggregate particles, the surface roughness will be high as well. Fig. 13b shows a representative picture of a concrete specimen tested at the fast loading rate (100 μm/min), where arrows point to fractured aggregate particles. In the specimens tested at the fast loading rates, most of the aggregate particles are fractured. For fracture of the potential bridging particles prior to full debonding, the toughening contribution is expected to be lower and a flatter fracture surface and lower surface roughness result. These microscopic observations of concrete fracture are in agreement with the results of mechanical and surface roughness measurements.

In a separate study performed on a grain-bridging ceramic material [23], coarse-grained alumina, resistance curve results, and fractographic observations were similar to that of concrete. At slow loading rates (0.25–1.0 μm/min), intergranular fracture transpires in coarse-grained alumina similar to crack growth around bridging aggregates in concrete. At fast loading rates (>10 μm/min), the fracture of alumina is characterized by an increasing degree of transgranular fracture analogous to fracture through aggregates in concrete. Fine-grained alumina examined in the same study showed negligible *R*-curve behavior and no rate effects, comparable to the present mortar observations. To explain this behavior, it is useful to examine the crack bridging process. Toughening by crack bridging is a combination of two events: debonding of the bridge from the surrounding material and frictional pullout of the bridging particle. From the work on alumina, we found that the rate dependence of toughness could be explained from a loading rate sensitive coefficient of friction between two sliding surfaces (for the bridge pullout contribution), and to a lesser extent by reduction in the number of bridges [23]. It is the latter which results in a flatter fracture surface. It is expected that a similar argument may be used to explain the rate-dependent behavior of concrete observed here, although the relative contributions of a rate-dependent friction coefficient and the reduction in the number of bridges are not specifically known for the cement-based systems. Roughness measurements would indicate that, in this case, the decrease in the number of bridging aggregates with increasing rate is overriding. It should also be noted that the effectiveness of a bridging particle is directly related to its size, and hence its ability to span the crack opening well behind the crack tip [24]. The lack of significant bridging and rate effects in both fine-grained alumina and mortar are consistent with this argument.

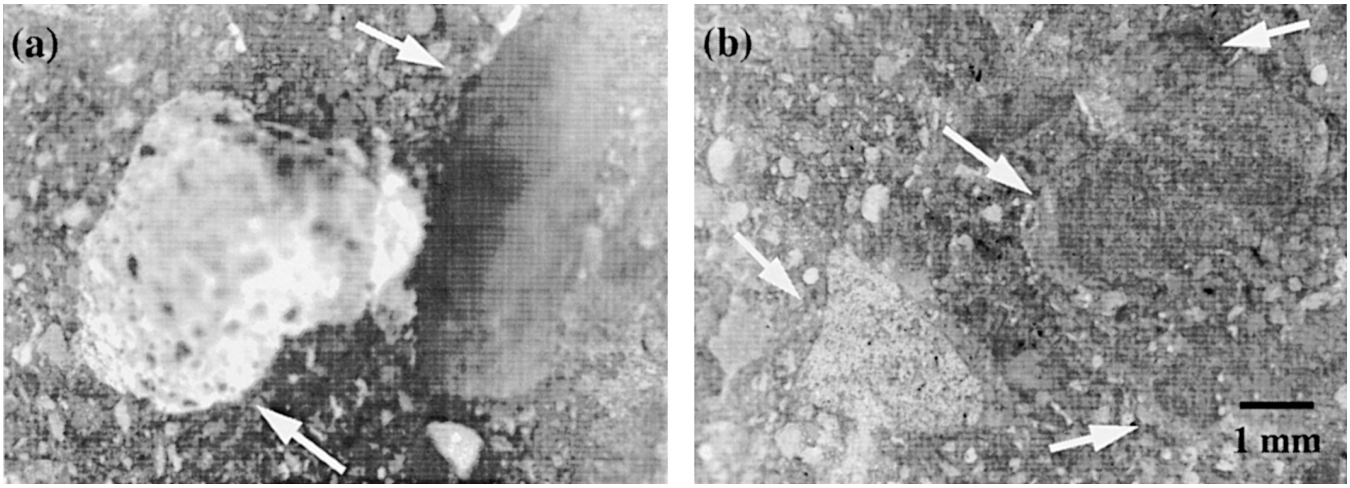

Fig. 13. (*a*) A representative picture of the fracture surface of a concrete specimen tested at the slow loading rate (0.25 μm/min). Arrows point to the unfractured aggregate particles left behind in the crack wake. (*b*) A representative picture of a concrete specimen tested at the fast loading rate (100 μm/min), where arrows point to fractured aggregate particles.

5. Summary

Experiments were performed to characterize the effect of loading rate on the toughening of cementitious materials. In cement paste and mortar, the K_{max} is independent of loading rate. In the case of concrete, the toughness decreases with increasing loading rate. Surface roughness measurements correlate well with fracture measurements. With an increase in loading rate, surface roughness of concrete surfaces diminishes, while the roughness of the paste and mortar are invariant with loading rate. Microscopic observations of the concrete surfaces show premature failure of aggregate particles at the high loading rates. Experiments performed on oven-dried mortar and concrete specimens demonstrate the same behavior, providing evidence that the observed effects are solely a loading rate phenomenon, and not creep related.

Appendix

The stress intensity factor (K_I) for a compact tension specimen [25] is given by Eq. (7) and Eq. (8):

$$K_I = \sigma\sqrt{\pi a}\, f\left(\frac{a}{W}\right) \tag{7}$$

where

$$f\left(\frac{a}{W}\right) = \left[\frac{1}{\left(1-\frac{a}{W}\right)^{3/2}}\right]\left[1.1214 + 0.0294\left(\frac{a}{W}\right) - 2.1907\left(\frac{a}{W}\right)^2 + 3.5511\left(\frac{a}{W}\right)^3 - 6.2459\left(\frac{a}{W}\right)^4 - 21.1853\left(\frac{a}{W}\right)^5 + 20.0463\left(\frac{a}{W}\right)^6 - 6.4967\left(\frac{a}{W}\right)^7\right] \tag{8}$$

and *COD* is given by Eqs. (9–12):

$$COD\left(\frac{a}{W},\frac{x}{W}\right) = \frac{\sigma a}{\sqrt{2WE}}\left(1-\frac{x}{a}\right)^{1/2}\left[F_1\left(\frac{a}{W}\right) + \left(1-\frac{x}{a}\right)F_2\left(\frac{a}{W}\right) + \left(1-\frac{x}{a}\right)^2 F_3\left(\frac{a}{W}\right)\right] \tag{9}$$

$$F_1\left(\frac{a}{W}\right) = 4f\left(\frac{a}{W}\right) \tag{10}$$

$$F_2\left(\frac{a}{W}\right) = \frac{35\sqrt{2}}{12}\pi\phi\left(\frac{a}{W}\right) - 8f\left(\frac{a}{W}\right) \tag{11}$$

$$F_3\left(\frac{a}{W}\right) = \frac{28}{15}f\left(\frac{a}{W}\right) - \frac{7\sqrt{2}}{12}\pi\phi\left(\frac{a}{W}\right) \tag{12}$$

Eq. (9) equals *CMOD* for $x = 0$ and $CTOD_c$ for $x = a_o$. The function *f(a/W)* is given by Eq. (8) and ϕ*(a/W)* is given as Eq. (13):

$$\phi\left(\frac{a}{W}\right) = \frac{1}{\left(\frac{a}{W}\right)^2}\int_0^{\frac{a}{W}} s[f(s)]^2 ds \tag{13}$$

where σ is crack face stress at the unloading point in the softening branch, E is the elastic modulus of the material, b is thickness of the specimen, W is width of the specimen, a is the crack length, and x is the coordinate direction along the crack growth.

Acknowledgments

This work was supported by the National Science Foundation Center for Advanced Cement Based Materials at Northwestern University. The authors wish to thank T.C. Easley for reading and assisting with the manuscript.

References

[1] S. Mindess, The fracture process zone in concrete, in: S.P. Shah (Ed.), Toughening Mechanisms in Quasi-Brittle Materials, Kluwer Academic Publishers, The Netherlands, 1991, pp. 271–286.
[2] L. Struble, P. Stutzman, E.R. Fuller Jr., J Am Ceram Soc 72 (1989) 2295
[3] A.K. Maji, C. Ouyang, S.P. Shah, J Mater Res 5 (1990) 206.
[4] J.G.M. Van Mier, Similarities between fracture processes in concrete, rock and ceramics, in: S.P. Shah (ed.), Toughening Mechanisms in Quasi-Brittle Materials, Kluwer Academic Publishers, The Netherlands, 1991, pp. 329–335.
[5] Y.S. Jenq, S.P. Shah, Eng Fract Mech 21 (1985) 1055.
[6] Y.S. Jenq, S.P. Shah, J Eng Mech 111 (1985) 1227.
[7] M. Wecharatana, S.P. Shah, Cem Concr Res 10 (1980) 833.
[8] D.A. Lange, H. Jennings, S.P. Shah, J Am Ceram Soc 76 (1993) 589.
[9] A.M. Hammad, M.A. Issa, New Experimental Techniques for Evaluating Materials and Structure Performances, American Concrete Institute, Detroit, 1991, pp. 191–200.
[10] E. Wollrab, C. Ouyang, S.P. Shah, J. Hamm, G. Konig, Mag Concr Res 48 (1996) 117.
[11] D.A. Abrams, Proc ASTM 17, Part II (1917) 364.
[12] D. Watstein, J ACI, 24 (1952) 729.
[13] S. Mindess, J.S. Nadeau, Ceram Bull 56 (1977) 429.
[14] Z.P. Bazant, R. Gettu, ACI Materials J, 89 (1992) 456.
[15] C-192, Standard Practice for Making and Curing Concrete Test Specimens in the Laboratory, ASTM, Philadelphia, PA, 1986, pp. 113–117.
[16] H. Tada, P.C. Paris, G.R. Irwin, The Stress Analysis of Cracks Handbook, Del Research Corp., Hellertown, PA, 1973.
[17] R. John, S.P. Shah, Y.-S. Jenq, Cem Concr Res, 17 (1987) 249.
[18] C. Ouyang, S.P. Shah, J Am Ceram Soc 74 (1991) 2831.
[19] Z.P. Bazant, Z. Moschovidis, J Am Ceram Soc 56 (1973) 235.
[20] H.F.W. Taylor, Cement Chemistry, Academic Press, New York, 1990, p. 272.
[21] J.J. Mecholsky, D.E. Passoja, K.S. Feinberg-Ringel, J Am Ceram Soc 72 (1989) 60.
[22] ANSI/ASME, Surface Texture (Surface Roughness, Waviness and Lay), B46.1, ASTM, Philadelphia, PA, 1985.
[23] S. Tandon, K.T. Faber, Acta Mater 46 (1998), 3547.
[24] S.J. Bennison, B.R. Lawn, Acta Metall Mater 37 (1989) 2659.
[25] X.-R. Wu, A.J. Carlsson, Weight Functions and Stress Intensity Factor Analysis, 1st ed., Pergamon Press, 1991.